Hindawi
Mathematical Problems in Engineering
Volume 2021, Article ID 9924427, 18 pages
https://doi.org/10.1155/2021/9924427

Research Article

Modeling and Optimizing the Effects of Insert Angles on Hard Turning Performance

Pham Minh Duc, Mai Duc Dai, and Le Hieu Giang

Faculty of Mechanical Engineering, Ho Chi Minh City University of Technology and Education, Ho Chi Minh City, Vietnam

Correspondence should be addressed to Pham Minh Duc; ducpm@hcmute.edu.vn

Received 26 March 2021; Revised 19 April 2021; Accepted 3 May 2021; Published 15 June 2021

Academic Editor: Xiaodong Sun

To analyze hard turning performance characteristics, a new mathematical model was developed for the hard turning process, and cutting force (CF), another important response for cutting machining, was also studied in the present work. The analysis of the mathematical model and experimental results revealed that thrust force (*Fy*) was the largest, followed by tangential force (*Fz*) and feed force (*Fx*). The resultant CF was most influenced by inclination angle (IA) with 25.02%, followed by rake angle (RA) (14.26%) and cutting edge angle (CEA) (10.04%). Increasing CEA changed the position of cutting on the tool-nose radius and increased local negative RA and correspondingly local clearance angle (CA). Meanwhile, increasing negative RA and IA resulted in larger local negative RA and CA. Moreover, local RA and local CA were the main geometric factors affecting surface roughness (SR), tool wear (TW), and CF. Increasing local negative RA resulted in higher SR and CF. In contrast, increasing local CA resulted in lower SR, TW, and CF. Under specific conditions, the positive effects of the local CA overcame the negative effects of the local negative RA, leading to a simultaneous decrease in SR and TW. The proposed novel mathematical model can be further applied to calculate local CF, cutting temperature, and TW for each cutting-edge element, to analyze and optimize the hard turning process.

1. Introduction

Hard turning is an advanced technology to machine hard materials and has many advantages compared to conventional grinding. However, the main problem of hard turning is the high surface roughness (SR) of the machined components and quick tool wear (TW). Because of large differences between conventional machining and hard turning, the existing theoretical calculations for the former are usually not applicable to the latter [1].

The tool geometry is crucial in hard turning because it affects the performance characteristics such as SR, TW, and CF. In our previously published study [2], we performed an experimental study on the influence of tool angles on SR and TW in hard turning. The results indicated that SR and TW were affected the most by IA. And Gökkaya and Nalbant studied the effects of the tool nose radius and cutting conditions on SR when turning with coated cemented carbide inserts [3]. A minimum SR was obtained with the highest tool-nose radius. The vibrations when using high tool-nose radii did not significantly affect SR. Therefore, high tool-nose radii were recommended for lower SR. From an experimental study on the effect of RA on CF, Günay et al. found that the main CF can be reduced by increasing positive RA and increased by increasing negative RA [4]. And Cao et al. also indicated that CF and SR decreased with increasing RA [5]. Zerti et al. used the Taguchi method to optimize CEA and insert nose radius, feed rate, cutting depth, and cutting speed in turning AISI steel [6]. The authors found that higher CEA and tool-nose radius reduced SR. Harisha et al. also used the Taguchi approach for experimental design and optimization of machining parameters, including CEA, cutting depth, feed rate, and tool nose radius to minimize CF when turning AISI 1055 hardened steel [7]. The authors found that the cutting depth and CEA were important factors on CF. When increasing the CEA, the feed force increased, while the thrust force decreased. CF increased with the feed rate. The optimal CEA was in the

range of 60°–70°. Saglam et al. studied the effect of feed rate, CEA, and RA on CF components and cutting temperature in hard turning of AISI 1040 hardened steel by uncoated cemented carbide tool [8]. The authors found that higher CEA produced lower thrust force and higher feed force, and increasing the positive RA decreased CF and increased the cutting temperature. And Singh and Rao investigated the influence of tool geometries, including nose radius and effective rake angle (RA), and machining parameters, including feed rate and cutting speed on SR when hard turning AISI 52100 steel with mixed ceramic inserts [9]. The results showed that higher effective negative RA and feed rate, lower nose radius, and cutting speed increased SR. Moreover, the influence of the feed rate and the insert nose radius on SR was consistent with the theoretical equation SR = $(f^2/32r)$. Neseli et al. also tried to optimize the tool geometry (tool-nose radius, RA, and CEA) on SR when turning AISI 1040 steel with Al_2O_3/TiC mixed ceramic inserts [10]. The most influencing factor on SR was the tool-nose radius, followed by CEA and RA. The SR increased with an increase in the CEA and negative back RA. However, the author found that higher tool-nose radii resulted in higher SR, which contradicts common expectations. Sharma et al. found that SR increases with feed rate but decreases with CEA, cutting speed and cutting depth when hard turning with coated carbide insert [11]. This means that the influences of CEA on SR in the studies of Neseli et al. and Sharma et al. were opposite, indicating that the influences of the tool geometry on conventional turning were different from the influences on hard turning. Sahoo and Sahoo investigated TW, SR, chip morphology, and CFs during hard turning of AISI 4340 steel using uncoated and multilayer-coated carbide inserts [12]. Experimental results showed that coated carbide insert was better than uncoated insert in terms of CF, SR, and TW.

On the other hand, Zhou et al. found that CF and tool life are strongly influenced by chamfer angle in hard turning, and cutting force increases with an increase in chamfer angle [13]. Zhao et al. assessed the effects of cutting-edge radius on surface quality and TW during hard turning of AISI 52100 steel tests [14]. The authors found that an increase in cutting-edge radius reduced TW. Xu et al. studied the hard machining of AISI 52100 steel and found that changing tool rake surface geometry significantly reduced cutting temperatures, CF, and residual stresses, compared to the flat tool [15]. However, it also lowered the strength of the cutting edge. In milling process, the tool geometry was also included in a cutter displacements (vibrations) model developed by Wojciechowski et al. [16].

Besides the tool geometry, cutting conditions such as cutting speed, cutting depth, and feed rate were shown to significantly affect the hard turning performance. For example, Suresh and Basavarajappa studied the effect of machining parameters (depth of cut, cutting speed, and feed rate) on TW and SR in hard turning AISI H13 steel (55 HRC) by coated ceramic inserts [17]. The results indicated that cutting speed mainly affected TW, while SR was most affected by feed rate. Rashid et al. found that when the feed rate was as low as 0.02 mm/rev, it was the most influencing factor on SR (99.16%). However, a low feed rate caused high TW, so the choice of feed rate must be reasonable between cost and quality [18]. In an experimental study on the hard turning of AISI 52100 steel with CBN inserts, Kumar found that the feed rate was the most important contributor to SR while cutting depth was the main factor on CF [19]. CF and SR increased with the increase in feed rate and cutting depth, while decreased with cutting speed. Khamel et al. used response surface methodology (RSM) combined with L27 Taguchi design to model the relationship between responses and cutting conditions during hard turning AISI 52100 steel [20]. Analysis of variance indicated that higher values of cutting depth, feed rate, and cutting speed reduced the tool life. The cutting speed was the most important for tool life, cutting depth was the most influential factor for CF, and feed rate was the main contributor to SR. Thrust force was the greatest component of CF. High cutting speeds resulted in high temperatures in the cutting zone, hence softened the machined materials and reduced the chip thickness and the length of tool-chip contact. The final results were decreases in SR and CF. Zerti et al. studied the effects of cutting speed, cutting depth, and feed rate on SR, CF, and rate of material removal (RMR) in hard turning AISI 420 hardened steel using Taguchi experimental design (L25) [21]. The result showed that SR was greatly affected by the feed rate, while the cutting depth had the most influence on the CF, the cutting power, and the RMR. RSM and artificial neural network (ANN) were used for modeling the machining performance with high accuracies. Chabbi et al. also used RSM and ANN to reveal the relationship between process parameters (cutting speed, feed rate, and cutting depth) and hard turning performance (SR, CF, and RMR) [22]. The determination coefficient of the ANN model was larger than that of the RSM. However, the RSM model is essential for ANOVA. Laouissi et al. compared SR, cutting power, tangential CF, and RMR when turning cast iron using coated and uncoated ceramic tools [23]. The coated tool showed lower SR and CF. The most influential factor on SR was feed rate, followed by cutting speed and cutting depth. The most influencing factor on CF was cutting depth, then feed rate, and cutting speed. RSM and desirability function (DF) were used to model and optimize the hard turning of AISI 316 steel using carbide inserts [24]. Feed rate was the major factor affecting SR, while cutting speed was the most influencing factor on TW. SR increased with higher cutting speeds and feed rates, while the TW increased with higher cutting speeds and cutting depths. The determination coefficients of the quadratic models were 90%, 93.5%, and 88.5% for power consumption, SR, and TW, respectively. Besides DF as a widely used multiobjective optimization method, different optimization techniques can be combined to increase optimal efficiency, such as multilevel strategy or combining fuzzy and sequential Taguchi methods [25, 26].

From the mathematical point of view, there were only a few studies on geometrical modeling of the hard turning process. For example, Bushlya et al. proposed the chip area and tool geometry models when oblique turning with round tools [27]. Khlifi et al. modeled the turning process by the equivalent cutting-edge, which theoretically induced the same CF components as the real tool [28]. And Orra and

Choudhury also used the equivalent cutting-edge concept to take into account the effects of cutting tool-nose radius [29]. In this context, equivalent angles and uncut chip thickness are defined. However, this approach is not suitable to study tool design and TW, where local data, e.g., temperature distribution at the rake face, are required. Abdellaoui and Bouzid developed a geometric model for the uncut chip area [30]. The cutting edge was decomposed into cutting-edge elements, and then the thickness of uncut chips, direction angle, and cutting depth were determined for each element. A thermomechanical model was applied for every cutting-edge element to determine cutting force components for each element. Molinari and Moufki also modeled the turning process with CEA lower than 90° [31]. To simulate the real cutting tool, its tool-nose radius was mathematically decomposed into straight cutting-edge elements with defined local geometry parameters. This approach was applied to calculate the global chip flow direction, the cutting temperature distribution, CF, and TW. Fu et al. proposed an analytical model where the real cutting-edge was decomposed into a series of infinitesimal cutting elements [32]. However, the mathematical models reported above described only the tool-nose radius as the major cutting-edge element, but did not describe the essence of hard turning and was limited in the number of elements.

The literature survey above showed that most studies focused on cutting conditions, while only a few investigated the tool geometry parameters, among which the tool angle is crucial for hard turning [33]. In this study, CF, another important response for cutting machining, was studied in the present work, and we proposed a new geometrical model to explain the effects of tool angle parameters on performance characteristics of hard turning, including SR, TW, and CF.

2. Experimental Procedure

2.1. Equipment and Materials. CNC lathe BOEHRINGER DUS-400ti with a spindle power of 11 kW was used for hard turning workpieces of AISI 1055 steel (HRC 52 ± 1) with a 53 mm diameter and 130 mm length using mixed ceramic inserts composed of 70% Al_2O_3 and 30% TiC and coated with PVD-TiN (Figure 1). A tool holder (ISO PTGNR 1616H 16) clamped the inserts (ISO TNGA160408S01525) with RA $\gamma_o = -6^\circ$, CEA $\kappa_r = 91^\circ$ and IA $\lambda_s = -6^\circ$. Both the tool holder and the inserts were purchased from Sandvik (Sweden). The cutting conditions were based on the catalog of the tool manufacturer: $v = 120$ m/min, $d_w = 0.2$ mm, and $f = 0.08$ mm/rev.

2.2. Methodology. RSM coupled with central composite design (CCD) was used to build a quadratic mathematical model:

$$Y = a_0 + \sum_{i=1}^{3} a_i X_i + \sum_{i=1}^{3} a_{ii} X_i^2 + \sum_{i<j}^{3} a_{ij} X_i X_j + \varepsilon, \tag{1}$$

where Y is the response (SR, TW, or CF); a_0 is the constant; a_i, a_{ii} and a_{ij} are the coefficients of linear, quadratic and interaction terms, respectively. X_i is the coded variables (CEA κ_r, RA γ_o and IA λ_s), and ε is the random experimental error. The experimental design based on CCD is shown in Table 1.

3. Modeling the Hard Turning Process

To analyze the effects of tool angle parameters on TW, SR, and CF with only the tool-nose radius engaging ($d_w \le r(1 - \cos K_r)$), the main cutting edge was considered as a cutting edge element ($j = 0$) and the engaged part of the tool-nose radius was modeled by decomposing into straight cutting edge elements (j) so that different models of CF, cutting temperature, TW, etc., can be applied to each element. The configuration in hard turning and local tool geometry parameters are shown in Figure 2. The cutting edge elements from θ_A to θ_C are the major, while the elements from θ_C to θ_D are the minor cutting edge.

3.1. Modeling the Tool Geometry. Now, we will define the local tool geometry parameters and the chip load of each cutting-edge element. The planes P_{s1}^j, P_{s-s}^j, and P_{o-o}^j are parallel to the tool cutting-edge plane of cutting-edge element (j) P_s^j, the tool cutting-edge plane P_s, and the orthogonal plane P_o, respectively, as Figure 3. The plane P_c is the tool rake plane; the planes P_n^j and P_o^j are the cutting-edge normal and orthogonal planes of cutting-edge element (j).

As follows from Figure 3,

Local cutting-edge angle:

$$\begin{aligned} K_r^j &= K_r - \theta^j, \quad \text{at } \theta^j \le K_r, \\ K_r^j &= \theta^j - K_r, \quad \text{at } \theta^j > K_r. \end{aligned} \tag{2}$$

Besides, we get

$$\tan \gamma_o^j = \frac{H}{L1}, \tag{3}$$

$$\begin{aligned} \Delta H2 &= L4 \tan \lambda_s^j, \\ \Delta H3 &= L3 \tan \lambda_s^j, \end{aligned} \tag{4}$$

$$\begin{aligned} \frac{L1}{L2} &= \sin\left(\frac{\pi}{2} - \theta^j\right), \\ \frac{L3}{L2} &= \cos\left(\frac{\pi}{2} - \theta^j\right), \\ \frac{L1}{L5} &= \cos\left(\frac{\pi}{2} - \theta^j\right), \\ \frac{L4}{L5} &= \sin\left(\frac{\pi}{2} - \theta^j\right), \end{aligned} \tag{5}$$

$$\begin{aligned} \tan \gamma_{o-o}^j &= \tan \gamma_o = \frac{H - \Delta H3}{L2}, \\ \tan \gamma_{s-s}^j &= \tan \lambda_s = \frac{H + \Delta H2}{L5}. \end{aligned} \tag{6}$$

Substituting equations (3)–(5) into equation (6), one obtains

Figure 1: Experimental setup.

Table 1: Levels of input variables based on CCD of experiments.

Input parameters	Level				
	$-\alpha$	-1	0	$+1$	$+\alpha$
Cutting edge angle (κ_r, °)	60	66	75	84	90
Rake angle (γ_o, °)	−2	−3.6	−6	−8.4	−10
IA (λ_s, °)	−2	−3.6	−6	−8.4	−10

$$\tan\gamma_o = \sin\left(\frac{\pi}{2} - \theta^j\right)\tan\gamma_o^j - \cos\left(\frac{\pi}{2} - \theta^j\right)\tan\lambda_s^j,$$
$$\tan\lambda_s = \cos\left(\frac{\pi}{2} - \theta^j\right)\tan\gamma_o^j + \sin\left(\frac{\pi}{2} - \theta^j\right)\tan\lambda_s^j. \quad (7)$$

These relationships have been derived using equation (7).

Local rake angle:

$$\gamma_o^j = \tan^{-1}\left(\sin\left(\frac{\pi}{2} - \theta^j\right)\tan\gamma_o + \cos\left(\frac{\pi}{2} - \theta^j\right)\tan\lambda_s\right). \quad (8)$$

Local inclination angle:

$$\lambda_s^j = \tan^{-1}\left(-\cos\left(\frac{\pi}{2} - \theta^j\right)\tan\gamma_o + \sin\left(\frac{\pi}{2} - \theta^j\right)\tan\lambda_s\right), \quad \text{at } \theta^j \le K_r,$$
$$\lambda_s^j = -\tan^{-1}\left(-\cos\left(\frac{\pi}{2} - \theta^j\right)\tan\gamma_o + \sin\left(\frac{\pi}{2} - \theta^j\right)\tan\lambda_s\right), \quad \text{at } \theta^j > K_r. \quad (9)$$

And local normal rake angle from local rake angle:

$$\tan\gamma_n^j = \tan\gamma_o^j \cos\lambda_s^j. \quad (10)$$

3.2. Modeling Undeformed Chip Area. From Figure 4, we get the engaged part in the cutting of the nose radius:

$$\begin{aligned}
\theta_A &= K_r - \angle AO_2E = K_r - \cos^{-1}\left(\frac{r-d_w}{r}\right),\\
\theta_C &= K_r,\\
\theta_D &= K_r + \angle CO_2D = K_r + \sin^{-1}\left(\frac{f}{2r}\right),\\
\theta_B &= K_r - \angle FO_2E = K_r - \tan^{-1}\left(\frac{AE-AF}{O_2E}\right) = K_r - \tan^{-1}\left(\frac{r\sin(K_r-\theta_A)-f}{r-d_w}\right).
\end{aligned} \tag{11}$$

Local uncut chip thickness:
Zone 1: $\theta_A \le \theta^j < \theta_B$.

$$t_1\left(\theta^j\right) = r - O_2X_1 = r - \frac{r-d_w}{\cos\left(K_r-\theta^j\right)}. \tag{12}$$

Zone 2: $\theta_B \le \theta^j \le \theta_D$.

$$t_2\left(\theta^j\right) = r - O_2X_2 = r - \sqrt{r^2+f^2-2rf\cos\angle O_2O_1X_2}. \tag{13}$$

Using the law of sines,

$$\begin{aligned}
\frac{O_1O_2}{\sin\angle O_2X_2O_1} &= \frac{O_1X_2}{\sin\angle O_1O_2X_2},\\
\frac{f}{\sin\left(\theta^j+(\pi/2)-K_r-\angle O_2O_1X_2\right)} &= \frac{r}{\sin\left(\pi-\left(\theta^j+(\pi/2)-K_r\right)\right)}.
\end{aligned} \tag{14}$$

The following relationship is obtained from equation (14):

$$\angle O_2O_1X_2 = \left(\theta^j+(\pi/2)-K_r-\sin^{-1}\left(\frac{f}{r}\sin\left(\theta^j+(\pi/2)-K_r\right)\right)\right). \tag{15}$$

Substituting equation (15) into equation (13), one obtains

$$t_2\left(\theta^j\right) = r - \sqrt{r^2+f^2-2rf\cos\left(\theta^j+\frac{\pi}{2}-K_r-\sin^{-1}\left(\frac{f}{r}\sin\left(\theta^j+\frac{\pi}{2}-K_r\right)\right)\right)}. \tag{16}$$

The corresponding local chip area is

$$\mathrm{d}A^j = t\left(\theta^j\right)\mathrm{d}\theta, \text{with an angular increment } \mathrm{d}\theta. \tag{17}$$

To calculate θ_c^j at the tool rake plane P_c, we use the coordinate transformation matrix:

The basis (z_c, y_c^j, x_c^j) is obtained from (z_c, y_c^o, x_c^o) by a rotation of angle θ_c around z_c, Figure 5(a):

$$\begin{bmatrix} z_c \\ y_c^j \\ x_c^j \end{bmatrix} = \begin{bmatrix} 1 & 0 & 0 \\ 0 & \cos\theta_c^j & \sin\theta_c^j \\ 0 & -\sin\theta_c^j & \cos\theta_c^j \end{bmatrix} \begin{bmatrix} z_c \\ y_c^o \\ x_c^o \end{bmatrix}, \tag{18}$$

$$y_c^j = \cos\theta_c^j y_c^o + \sin\theta_c^j x_c^o.$$

The basis (x_r, y_r^j, x_r^j) is obtained from (x_r, y_r^o, x_r^o) by a rotation of angle θ_r around z_r (Figure 5(b)):

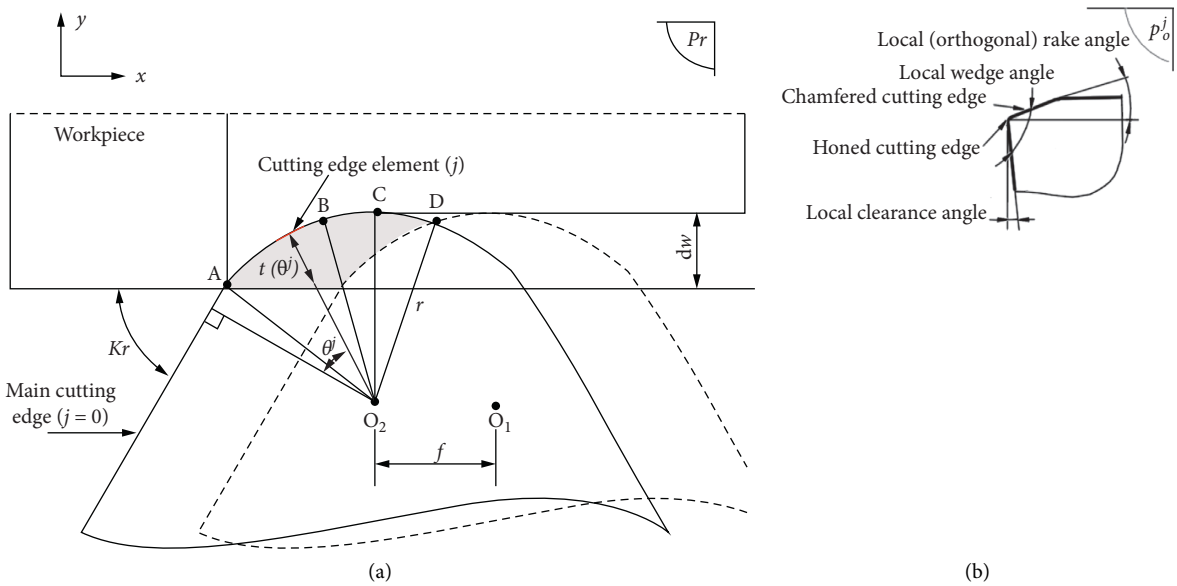

Figure 2: (a) The configuration of hard turning. (b) The tool geometry of cutting-edge element (j).

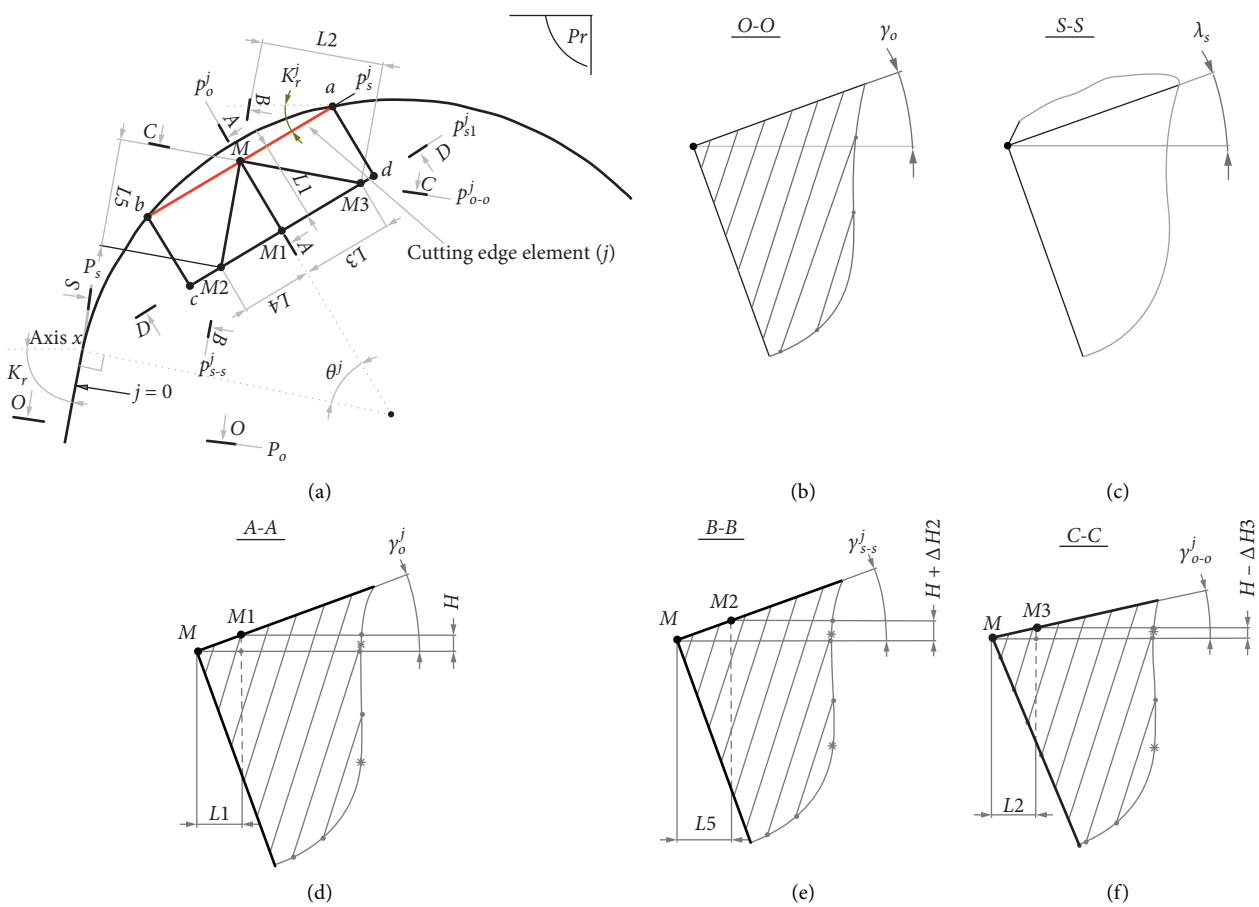

Figure 3: Continued.

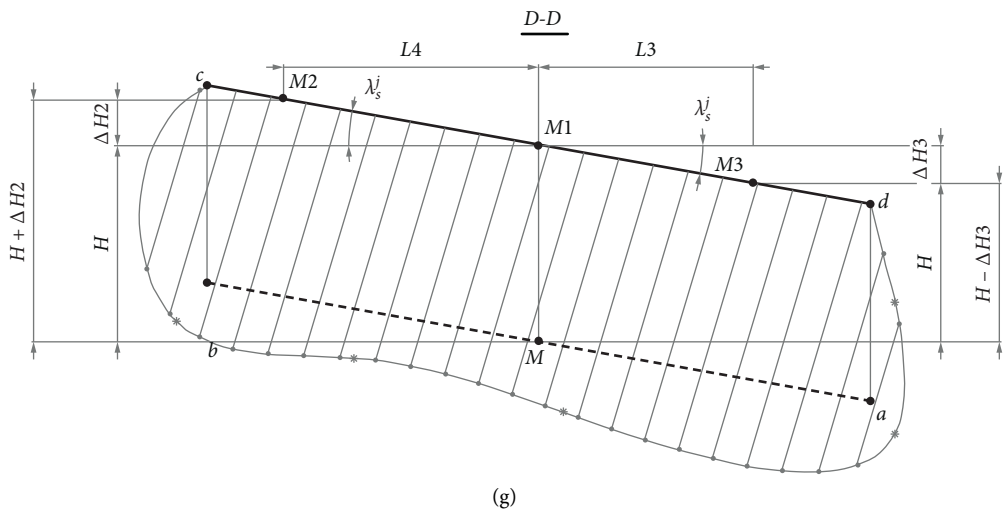

Figure 3: Model to correlate angles of the main cutting edge and cutting-edge elements (j).

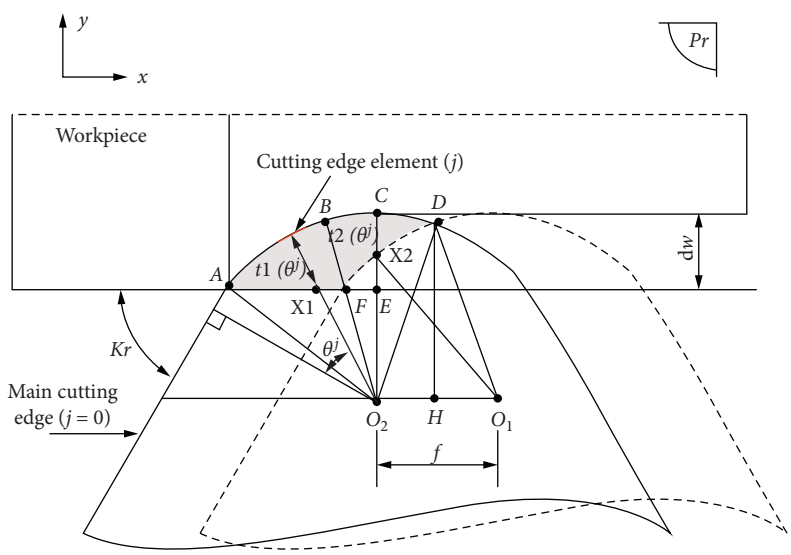

Figure 4: The local chip thickness of each cutting-edge element.

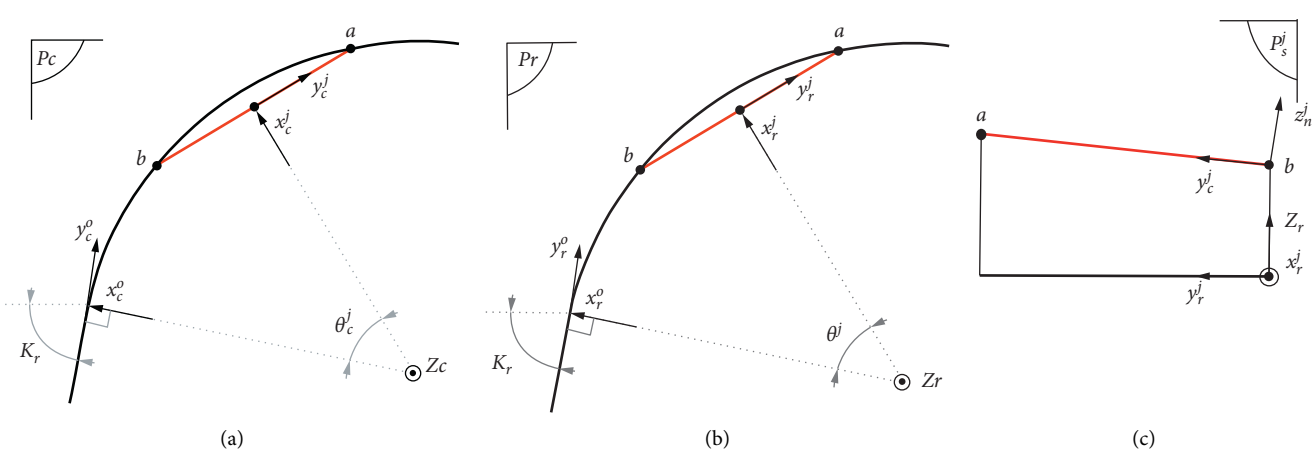

Figure 5: Continued.

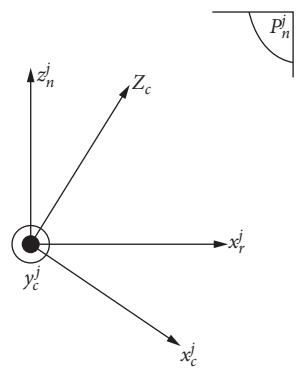

(d)

Figure 5: Relationships between systems: (a) (z_c, y_c^j, x_c^j) and (z_c, y_c^o, x_c^o) on the tool rake plane P_c; (b) (x_r, y_r^j, x_r^j) and (x_r, y_r^o, x_r^o) on the reference plane P_r; (c) (z_n^j, y_c^j, x_r^j) and (z_r, y_r^j, x_r^j) on the cutting-edge plane (j) P_s^j; and (d) (z_c, y_c^j, x_c^j) and (z_n^j, y_c^j, x_r^j) on the normal plane (j) P_n^j.

$$\begin{bmatrix} z_r \\ y_r^j \\ x_r^j \end{bmatrix} = \begin{bmatrix} 1 & 0 & 0 \\ 0 & \cos\theta^j & \sin\theta^j \\ 0 & -\sin\theta^j & \cos\theta^j \end{bmatrix} \begin{bmatrix} z_r \\ y_r^o \\ x_r^o \end{bmatrix}, \qquad y_r^j = \cos\theta^j y_r^o + \sin\theta^j x_r^o. \tag{19}$$

The basis (z_n^j, y_c^j, x_r^j) is obtained from (z_r, y_r^j, x_r^j) by a rotation of angle λ_s^j around x_s^j (Figure 5(c)):

$$\begin{bmatrix} z_n^j \\ y_c^j \\ x_r^j \end{bmatrix} = \begin{bmatrix} \cos\lambda_s^j & \sin\lambda_s^j & 0 \\ -\sin\lambda_s^j & \cos\lambda_s^j & 0 \\ 0 & 0 & 1 \end{bmatrix} \begin{bmatrix} z_r \\ y_r^j \\ x_r^j \end{bmatrix}, \qquad \begin{aligned} z_n^o &= \cos\lambda_s^o z_r + \sin\lambda_s^o y_r^o, \\ y_c^o &= -\sin\lambda_s^o z_r + \cos\lambda_s^o y_r^o. \end{aligned} \tag{20}$$

The basis (z_c, y_c^j, x_c^j) is obtained from (z_n^j, y_c^j, x_r^j) by a rotation of angleγ_n^j around y_c^j, Figure 5(d):

$$\begin{bmatrix} z_c \\ y_c^j \\ x_c^j \end{bmatrix} = \begin{bmatrix} \cos\gamma_n^j & 0 & -\sin\gamma_n^j \\ 0 & 1 & 0 \\ \sin\gamma_n^j & 0 & \cos\gamma_n^j \end{bmatrix} \begin{bmatrix} z_n^j \\ y_c^j \\ x_r^j \end{bmatrix}, \qquad x_c^o = \sin\gamma_n^o z_n^o + \cos\gamma_n^o x_r^o. \tag{21}$$

By substituting equations (20) and (21) into equation (18), we get

$$\begin{aligned} y_c^j &= \left(-\cos\theta_c^j \sin\lambda_s^o + \sin\theta_c^j \sin\gamma_n^o \cos\lambda_s^o\right) z_r + \left(\cos\theta_c^j \cos\lambda_s^o + \sin\theta_c^j \sin\gamma_n^o \sin\lambda_s^o\right) y_r^o + \sin\theta_c^j \sin\gamma_n^o x_r^o, \\ \text{or } y_c^j &= A z_r + B y_r^o + C x_r^o, \\ \text{with } A &= \left(-\cos\theta_c^j \sin\lambda_s^o + \sin\theta_c^j \sin\gamma_n^o \cos\lambda_s^o\right), \\ B &= \left(\cos\theta_c^j \cos\lambda_s^o + \sin\theta_c^j \sin\gamma_n^o \sin\lambda_s^o\right), \\ C &= \sin\theta_c^j \cos\gamma_n^o. \end{aligned} \tag{22}$$

And, y_r^j is the unit vector of the projection of cutting-edge element (j) on the reference plane (Pr). Therefore,

$$y_r^j = \frac{y_c^j - \left(y_c^j . z_r\right) z_r}{\left\| y_c^j - \left(y_c^j . z_r\right) z_r \right\|}. \tag{23}$$

Substituting equations (19) and (22) in to equation (23), we get

$$\cos\theta^j y_r^o + \sin\theta^j x_r^o = \frac{B y_r^o + C x_r^o}{X}, \quad \text{with } X = \left\| y_c^j - \left(y_c^j . z_r\right) z_r \right\|. \tag{24}$$

Then, after some algebraic manipulation we get

$$\tan\theta^j = \frac{\tan\theta_c^j \cos\gamma_n^o}{\cos\lambda_s^o + \tan\theta_c^j \sin\gamma_n^o \sin\lambda_s^o} = \frac{\tan\theta_c^j \cos\gamma_n}{\cos\lambda_s + \tan\theta_c^j \sin\gamma_n \sin\lambda_s}, \tag{25}$$

$$\theta_c^j = \tan^{-1}\left(\frac{\tan\theta^j \cos\lambda_s}{\cos\gamma_n - \tan\theta^j \sin\gamma_n \sin\lambda_s}\right), \quad \text{at } \theta^j < \frac{\pi}{2},$$

$$\theta_c^j = \tan^{-1}\left(\frac{\tan\theta^j \cos\lambda_s}{\cos\gamma_n - \tan\theta^j \sin\gamma_n \sin\lambda_s}\right) + \pi, \quad \text{at } \theta^j > \frac{\pi}{2}. \tag{26}$$

Summary of the modeling hard turning process is as follows.

Local cutting-edge angle:

$$K_r^j = K_r - \theta^j, \quad \text{at } \theta^j \le K_r,$$
$$K_r^j = \theta^j - K_r, \quad \text{at } \theta^j > K_r. \tag{27}$$

Local rake angle:

$$\gamma_o^j = \tan^{-1}\left(\sin\left(\frac{\pi}{2} - \theta^j\right)\tan\gamma_o + \cos\left(\frac{\pi}{2} - \theta^j\right)\tan\lambda_s\right). \tag{28}$$

Local normal rake angle:

$$\tan\gamma_n^j = \tan\gamma_o^j \cos\lambda_s. \tag{29}$$

Local inclination angle:

$$\lambda_s^j = \tan^{-1}\left(-\cos\left(\frac{\pi}{2} - \theta^j\right)\tan\gamma_o + \sin\left(\frac{\pi}{2} - \theta^j\right)\tan\lambda_s\right), \quad \text{at } \theta^j \le K_r,$$

$$\lambda_s^j = -\tan^{-1}\left(-\cos\left(\frac{\pi}{2} - \theta^j\right)\tan\gamma_o + \sin\left(\frac{\pi}{2} - \theta^j\right)\tan\lambda_s\right), \quad \text{at } \theta^j > K_r. \tag{30}$$

The engaged part in the cutting of the nose radius:

$$\theta_A = K_r - \cos^{-1}\left(\frac{r - d_w}{r}\right),$$
$$\theta_C = K_r,$$
$$\theta_D = K_r + \sin^{-1}\left(\frac{f}{2r}\right), \tag{31}$$
$$\theta_B = K_r - \tan^{-1}\left(\frac{r\sin(K_r - \theta_A) - f}{r - d_w}\right).$$

Angle θ_c^j in the tool rake plane:

$$\theta_c^j = \tan^{-1}\left(\frac{\tan\theta^j \cos\lambda_s}{\cos\gamma_n - \tan\theta^j \sin\gamma_n \sin\lambda_s}\right), \quad \text{at } \theta^j < \frac{\pi}{2},$$

$$\theta_c^j = \tan^{-1}\left(\frac{\tan\theta^j \cos\lambda_s}{\cos\gamma_n - \tan\theta^j \sin\gamma_n \sin\lambda_s}\right) + \pi, \quad \text{at } \theta^j > \frac{\pi}{2}. \tag{32}$$

Local uncut chip thickness:

Zone 1: $\theta_A \le \theta^j < \theta_B$

$$t_1(\theta^j) = r - \frac{r - d_w}{\cos(K_r - \theta^j)}. \tag{33}$$

Zone 2: $\theta_B \le \theta^j \le \theta_D$

$$t_2(\theta^j) = r - \sqrt{r^2 + f^2 - 2rf\cos\left(\theta^j + \frac{\pi}{2} - K_r - \sin^{-1}\left(\frac{f}{r}\sin\left(\theta^j + \frac{\pi}{2} - K_r\right)\right)\right)}. \tag{34}$$

The corresponding local chip area is. $dA^j = t(\theta^j) r\, d\theta$ with an angular increment $d\theta$

3.3. Comparison between the Mathematical Model and Real Cutting Process. To evaluate the accuracy of the mathematical model, we compared the calculated results with the experimental results for the hard turning at various conditions. For example, consider CEA $K_r = 84^\circ$, RA $\gamma_o = -6.03^\circ$, IA $\lambda_s = -6^\circ$, tool-nose radius $r = 0.8$ mm, chamfer angle $= 0^\circ$, cutting speed $v = 120$ m/min, cutting depth $d_w = 0.2$ mm, and feed rate $v = 0.08$ mm/rev. The calculated engaged part of the tool-nose radius was from $\theta_A = 42.59^\circ$ to $\theta_D = 86.87^\circ$, the local tool geometry parameters of the straight cutting edge element (j) (θ_A=42.59°) were the local CEA $K_r^j = 41.41^\circ$, the local RA $\gamma_o^j = -8.47^\circ$, IA $\lambda_s^j = -0.34^\circ$, and the local uncut chip thickness $t^j = 0$. At the cutting edge element j (θ_B=47.18°), the maximum undeformed chip thickness was $t^j = 0.05$ mm. The real cutting process (Figure 6) showed that the new mathematical model of the hard turning was accurate, and compared with the conventional mathematical model [30–32], our new model described the essence of the hard turning process and was not limited in the number of elements and CEA.

4. Analysis of the Mathematical Model and Experimental Results

4.1. Analysis of the Mathematical Model. Hard turning usually uses small cutting depths of 0.1-0.2 mm [34]. Based on the experimental results and the mathematical model of hard turning, we found that the cutting occurred only at the corner of tool-nose radius. Changing CEA resulted in a change in the cutting position on tool-nose radius (Figures 7(e) and 7(f) and Figure 8). Figures 7(a)–7(d) also show that, at a given cutting-edge element on the tool-nose radius, changing RA mainly caused a change in the local IA, while changing IA mainly caused a change in the local RA.

Based on the mathematical model, we can determine the change of local tool angles when changing the insert angle parameters as shown in Figure 7.

4.2. Analysis of the Experimental Results

4.2.1. CF Analysis. CF was measured in three directions, including feed force (Fx), thrust force (Fy), and tangential

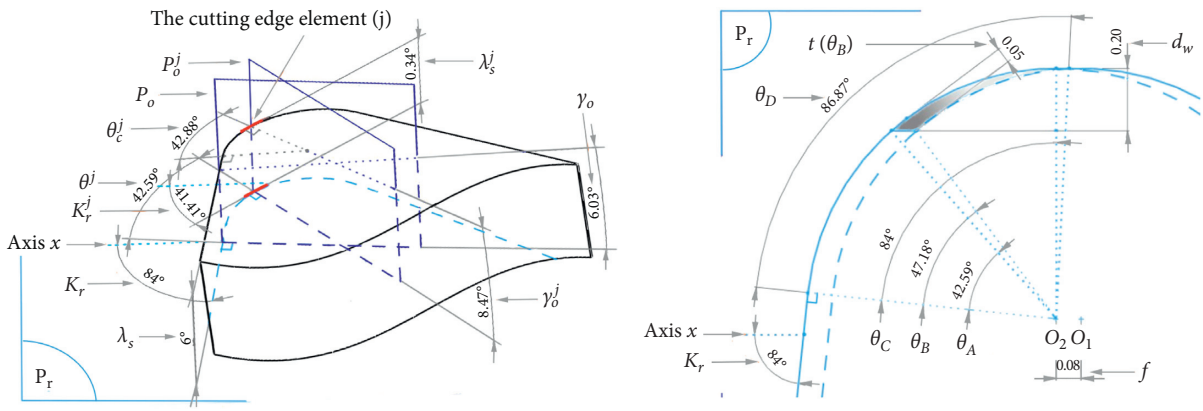

(a) (b)

Figure 6: The real cutting process in hard turning with $K_r = 84^\circ$, RA $\gamma_o = -6.03^\circ$, IA $\lambda_s = -6^\circ$, $r = 0.8$ mm, $d_w = 0.2$ mm, and $f = 0.08$ mm/rev. (a) The local tool geometry and (b) the uncut chip thickness parameters of the cutting edge element (j).

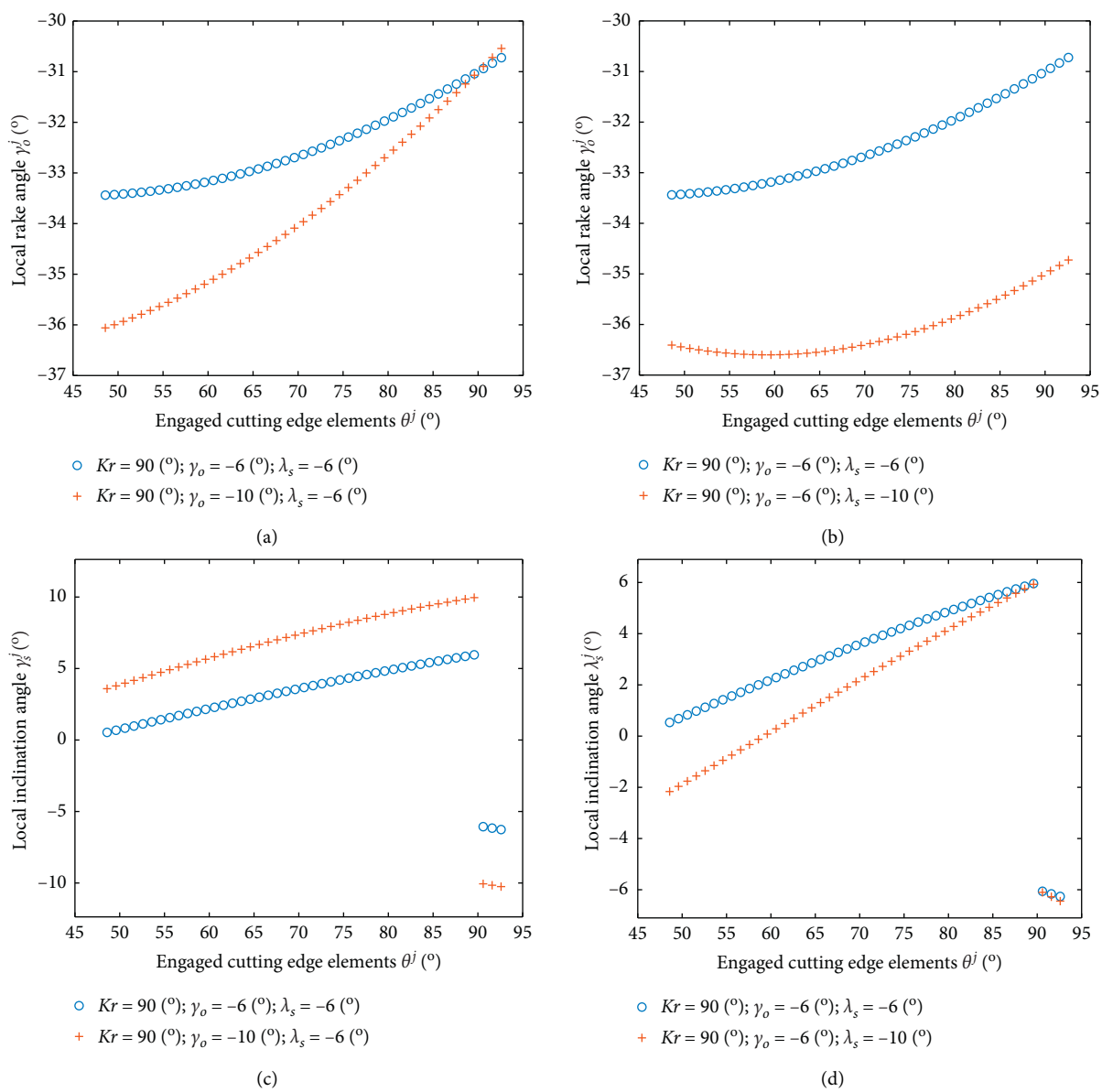

Figure 7: Continued.

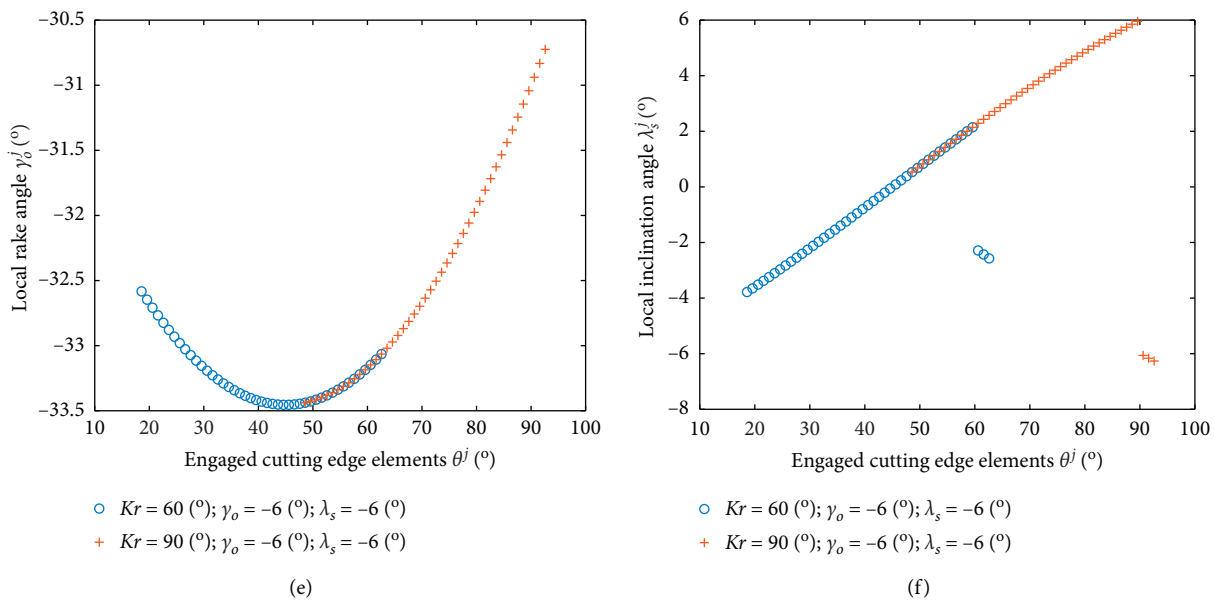

Figure 7: The local IA and RA when increasing RA, IA, and CEA, with chamfer angle = 25° and cutting conditions: dw = 0.2, f = 0.08, r = 0.8. (a) Local RA of engaged cutting-edge elements as increasing RA. (b) Local RA of engaged cutting-edge elements as increasing IA. (c) Local IA of engaged cutting-edge elements as increasing RA. (d) Local IA of engaged cutting-edge elements as increasing IA. (e) Local RA of engaged cutting-edge elements as increasing CEA. (f) Local IA of engaged cutting-edge elements as increasing CEA.

force (Fz) using a dynamometer (Kistler, 9257B) equipped with an amplifier (Kistler, 5070A) and a computer.

Table 2 shows that the thrust force (Fy) was the largest CF component, the tangential force (Fz) is the middle one and the feed force (Fx) is the smallest CF component, which was in accordance with previous works Khamel et al. [20], Azizi et al. [35], and Bouacha [36]. Due to the low cutting depth and feed rate during hard turning, CFs were usually small and had negligible influences on SR. However, there was a relationship between CF and TW. As in the 13th experiment, the CF and TW were the greatest, but the SR was the smallest.

Figure 9 shows the main effect and interaction effect plots for the resultant force. Figure 9(a) shows that CF decreased when the negative IA and RA increased. However, when IA increased higher than −7.2°, CF increased. Base on the mathematical model, this result was because the increase in the negative IA and RA led to higher local negative RA, which in turn increased the local CA (Figure 2(b)). Moreover, the increase due to IA was the largest (Figures 7(a) and 7(b)). Therefore, normal and friction forces on the tool rake face increased but these forces on the clearance face decreased, hence reaching a balance at IA of -7.2° with a minimum CF.

In our previous study, SR and TW were affected the most by IA. From Table 3–Table 6, IA was also the most important contributor to the CF components (Fx, Fy, and Fz) and resultant CF (F). From the mathematical model, IA was the major factor affecting local RA (and correspondingly local CA). And, the performance characteristics (SR, TW, and CF) of hard turning were affected by these local angles.

The regression equations for F, F_z, F_y, and F_x in terms of the cutting angles were

$$\begin{aligned}
F &= -48.3 + 5.325\kappa_r - 6.26\gamma_o + 5.36\lambda_s - 0.02697\kappa_r * \kappa_r - 0.1811\gamma_o * \gamma_o + 0.6273\lambda_s * \lambda_s + 0.0942\kappa_r * \gamma_o \\
&\quad + 0.0739\kappa_r * \lambda_s + 0.296\gamma_o * \lambda_s \left(R^2 = 95.52\%\right), \\
Fy &= 35.1 + 2.62\kappa_r - 2.16\gamma_o + 6.64\lambda_s - 0.00976\kappa_r * \kappa_r + 0.111\gamma_o * \gamma_o + 0.712\lambda_s * \lambda_s + 0.0894\kappa_r * \gamma_o \\
&\quad + 0.0708\kappa_r * \lambda_s + 0.329\gamma_o * \lambda_s \left(R^2 = 93.19\%\right), \\
Fz &= -39.0 + 3.071\kappa_r - 3.18\gamma_o + 0.61\lambda_s - 0.01666\kappa_r * \kappa_r - 0.1486\gamma_o * \gamma_o + 0.1974\lambda_s * \lambda_s + 0.0321\kappa_r * \gamma_o \\
&\quad + 0.0381\kappa_r * \lambda_s + 0.0857\gamma_o * \lambda_s \left(R^2 = 94.35\%\right), \\
Fx &= -171.2 + 5.067\kappa_r - 9.53\gamma_o - 0.23\lambda_s - 0.03249\kappa_r * \kappa_r - 0.6250\gamma_o * \gamma_o - 0.1034\lambda_s * \lambda_s + 0.0220\kappa_r * \gamma_o \\
&\quad - 0.0093\kappa_r * \lambda_s - 0.0344\gamma_o * \lambda_s \left(R^2 = 95.43\%\right).
\end{aligned} \tag{35}$$

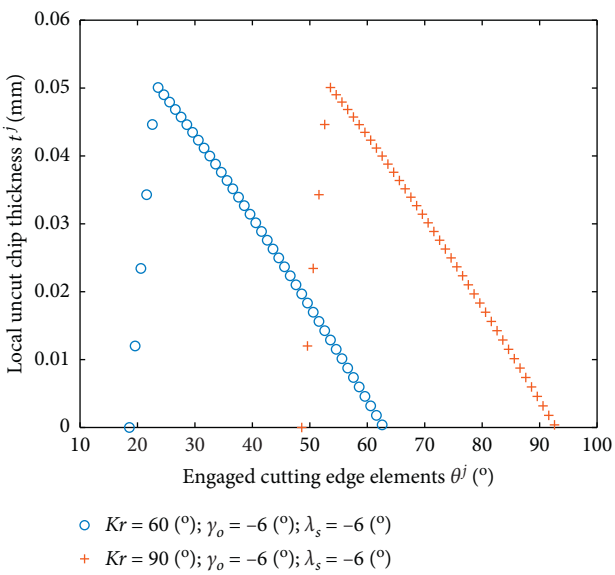

Figure 8: The local uncut chip thickness of engaged cutting-edge elements as increasing CEA, with cutting conditions: $d_w = 0.2$ mm, $f = 0.08$ mm/rev, $r = 0.8$ mm.

Table 2: Experimental results based on CCD.

κ_r (°)	γ_o (°)	λ_s (°)	Fx (N)	Fy (N)	Fz (N)	F (N)	Ra (μm)	VB (μm)
84	−3.6	−3.6	47.19	134.92	90.91	169.4	0.279	44.04
66	−3.6	−3.6	45.52	123.68	84.44	156.52	0.730	44.82
84	−8.4	−3.6	47.11	122.86	86.24	157.33	0.594	35.98
66	−8.4	−3.6	46.02	118.23	83.28	151.76	0.866	32.24
84	−3.6	−8.4	45.47	122.67	85.13	156.08	0.720	31.24
66	−3.6	−8.4	41.67	116.44	82.68	148.76	0.899	32.00
84	−8.4	−8.4	43.28	117.09	83.17	150	1.004	30.12
66	−8.4	−8.4	42.7	119.69	82.76	151.65	0.890	23.54
90	−6.0	−6.0	46	119.87	84.8	153.87	0.836	37.80
60	−6.0	−6.0	41.64	117.28	81.14	148.56	0.995	29.27
75	−2.0	−6.0	39.19	128.71	86.89	160.16	0.766	42.11
75	−10.0	−6.0	43.07	116.37	81.79	148.62	1.020	27.70
75	−6.0	−2.0	50.69	139	92.28	174.38	0.252	50.26
75	−6.0	−10.0	48.26	125.33	87.47	160.27	0.767	22.20
75	−6.0	−6.0	50.67	118.66	87.13	155.69	0.870	31.85
75	−6.0	−6.0	51.75	119.92	85.59	156.16	0.853	32.01
75	−6.0	−6.0	50.72	120.02	87.02	156.68	0.852	32.32
75	−6.0	−6.0	52.91	118.47	86.88	156.15	0.906	32.93
75	−6.0	−6.0	52.07	118.44	85.11	154.86	0.919	31.63
75	−6.0	−6.0	50.83	118.56	85.45	154.73	0.876	31.92

The determination coefficients R^2 for F, F_z, F_y, and F_x were high enough for reliable estimates.

4.2.2. TW Analysis. Under our cutting conditions (0.2 mm cutting depth, 0.08 mm/rev feed rate, and 0.8 mm nose radius), the mathematical model revealed that the cutting occurred only at the tool-nose radius corner. This result was in accordance with the experimental results that the TW occurred only at the tool-nose radius corner.

Figure 10(a) shows that the flank wear decreased when CEA decreased from 90° to 60° and RA, IA increased in the negative direction. The reason for this effect could be due to higher local negative RA and local CA resulted when decreasing CEA (Figure 7(e)) and increasing RA and IA (Figures 7(a) and 7(b)). This increase in the local CA finally resulted in less contact and less friction between the machined surface and the flank face because of the springback of the workpiece.

4.2.3. SR Analysis. From our previous investigation [2], the results showed that as the negative IA and RA increased and CEA changed from 90° to 60°, SR also increased. But IA continued to increase over −8.1°, and SR decreased (Figure 10(a)). Based on the proposed geometrical model, the reason for these results was that decreasing CEA and increasing negative IA and RA led to higher local negative RA and higher local CA (Figure 2(b)), with the increase due to IA was the largest (Figures 7(a) and 7(b)). An increase in the local negative RA resulted in a longer tool-chip contact and a higher ratio of chip compression, which caused more vibrations and subsequently higher SR. Oppositely, larger local CA reduced the tool-machined surface contact and the friction because of the springback of the workpiece [37], thus generating less vibration and lower SR. Under specific conditions, positive influences of local CA outplayed the negative influences of local negative RA, thus decreasing SR.

4.3. Multiobjective Optimization. Another goal of this research was to optimize the tool angle parameters to obtain multiple objectives based on SR, TW, and CF. The desirability function approach was used with the desirability function (D) defined as follows:

$$D = \left(\prod_{i=1}^{n} d_i \right)^{(1/n)}. \tag{36}$$

In the first case, it is desired to obtain target values of SR, TW, and CF. The desirability, in this case, is assigned as follows:

$$d_i = \begin{cases} 0, & \text{at } Y_i < \text{Low}_i, \\ \left(\dfrac{Y_i - \text{Low}_i}{\text{Tar}_i - \text{Low}_i} \right)^r, & \text{at Low}_i \le Y_i < \text{Tar}_i, \\ \left(\dfrac{\text{High}_i - Y_i}{\text{High}_i - \text{Tar}_i} \right)^r, & \text{at Tar}_i \le Y_i \le \text{High}_i, \\ 0, & \text{at } Y_i > \text{High}_i, \end{cases} \tag{37}$$

where d_i is the desirability derived from responses Y_i (SR, TW, and CF) and ranges from 0 to 1 (from least to most desired), $n = 3$ is the number of responses, and r is a parameter determining the form of d_i. Table 7 shows the results of multiobjective optimization for TW, SR, and CF.

Under optimized tool angle parameters in Table 7 (CEA $\kappa_r = 75°$, RA $\gamma_o = -6°$, and IA $\lambda_s = -10°$), the measured SR, flank wear, and CF were $Ra = 0.767$ μm, $VB = 22.2$ μm,

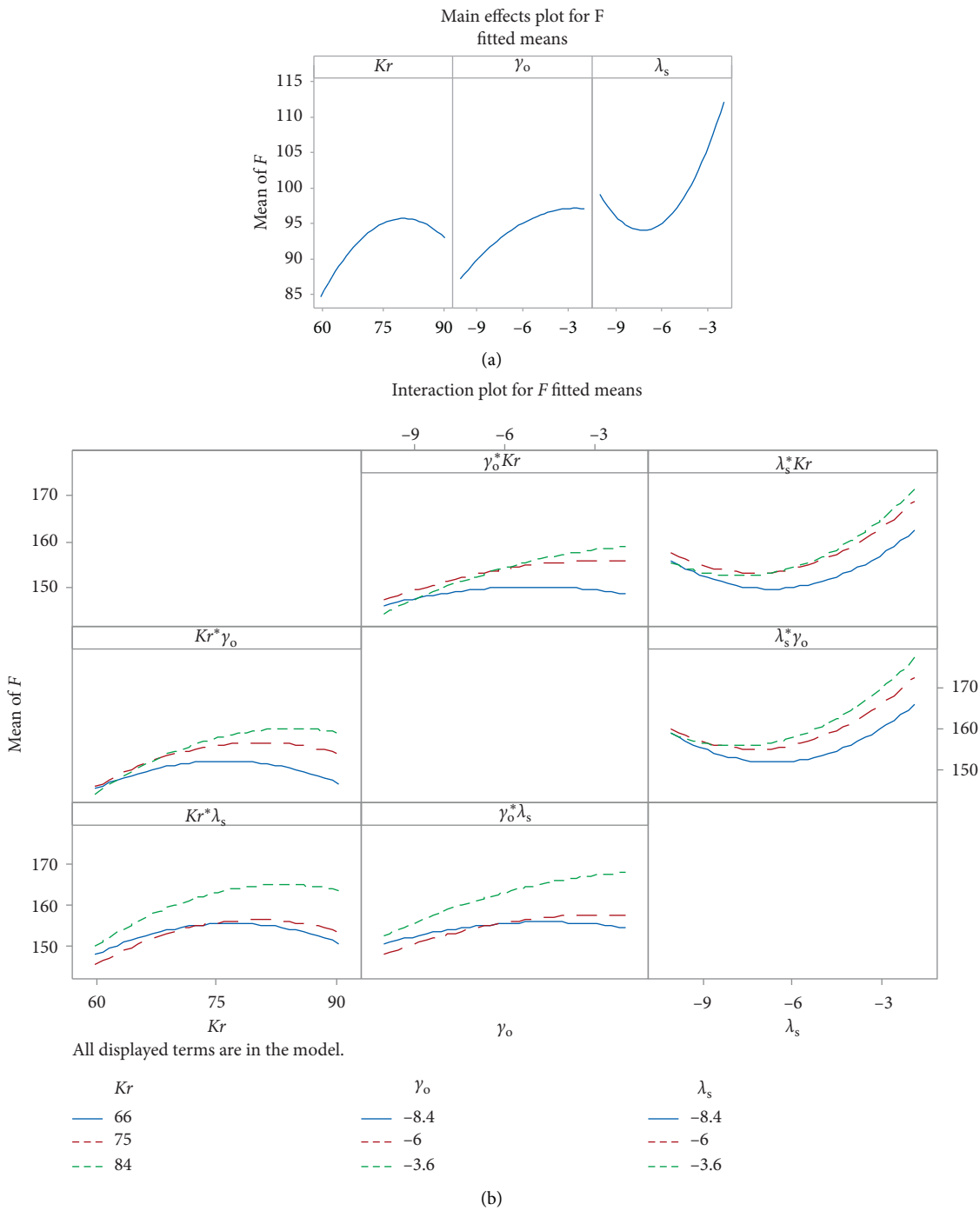

Figure 9: Main and interaction effects of tool angle parameters on CF (F).

and $F = 160.27$ N. Compared to the respective $Ra = 0.836\,\mu$m, $VB = 37.8\,\mu$m, and $F = 153.87$ N, when using standard tool parameters ($\kappa_r = 91^\circ$, $\gamma_o = -6^\circ$ and $\lambda_s = -6^\circ$), SR and TW decreased by 8.3% and 41.3%, respectively, while CF increased by 4%. Because CF is not an important output when considering optimal conditions for hard turning, these improvements in SR and TW have significant practical implications. Figure 11 shows the comparison between standard and optimized local tool angles.

In the second case, it is desired to attain the lowest TW, SR, and CF, so equation (38) was used.

$$d_i = \begin{cases} 1, & \text{at } Y_i < \text{Low}_i, \\ \left(\dfrac{\text{High}_i - Y_i}{\text{High}_i - \text{Low}_i}\right)^r, & \text{at } \text{Low}_i \le Y_i \le \text{High}_i, \\ 0, & \text{at } Y_i > \text{High}_i. \end{cases} \tag{38}$$

Table 3: Analysis of variance for CF (F).

Source	DF	Seq SS	Contribution (%)	Adj SS	Adj MS	F value	P value
Model	9	762.048	95.52	762.048	84.672	23.70	<0.0001
Linear	3	393.520	49.33	393.520	131.173	36.72	<0.0001
κ_r	1	80.132	10.04	80.132	80.132	22.43	0.001
γ_o	1	113.801	14.26	113.801	113.801	31.86	<0.0001
λ_s	1	199.587	25.02	199.587	199.587	55.87	<0.0001
Square	3	291.768	36.57	291.768	97.256	27.22	<0.0001
κ_r * κ_r	1	81.986	10.28	66.961	66.961	18.74	0.001
γ_o*γ_o	1	26.617	3.34	15.262	15.262	4.27	0.066
λ_s*λ_s	1	183.165	22.96	183.165	183.165	51.27	<0.0001
2-way interaction	3	76.761	9.62	76.761	25.587	7.16	0.007
κ_r *γ_o	1	33.120	4.15	33.120	33.120	9.27	0.012
κ_r *λ_s	1	20.408	2.56	20.408	20.408	5.71	0.038
γ_o*λ_s	1	23.232	2.91	23.232	23.232	6.50	0.029
Error	10	35.723	4.48	35.723	3.572		
Lack-of-fit	5	32.703	4.10	32.703	6.541	10.83	0.010
Pure error	5	3.021	0.38	3.021	0.604		
Total	19	797.772	100.00				

Table 4: Analysis of variance for thrust CF (Fy).

Source	DF	Seq SS	Contribution	Adj SS	Adj MS	F value	P value
Model	9	656.899	93.19	656.899	72.989	15.22	<0.0001
Linear	3	322.450	45.75	322.450	107.483	22.41	<0.0001
κ_r	1	41.849	5.94	41.849	41.849	8.72	0.014
γ_o	1	120.399	17.08	120.399	120.399	25.10	0.001
λ_s	1	160.202	22.73	160.202	160.202	33.40	<0.0001
Square	3	257.098	36.47	257.098	85.699	17.86	<0.0001
κ_r * κ_r	1	20.015	2.84	8.759	8.759	1.83	0.206
γ_o*γ_o	1	0.989	0.14	5.703	5.703	1.19	0.301
λ_s*λ_s	1	236.093	33.49	236.093	236.093	49.22	<0.0001
2-way interaction	3	77.352	10.97	77.352	25.784	5.37	0.018
κ_r *γ_o	1	29.807	4.23	29.807	29.807	6.21	0.032
κ_r *λ_s	1	18.733	2.66	18.733	18.733	3.91	0.076
γ_o*λ_s	1	28.812	4.09	28.812	28.812	6.01	0.034
Error	10	47.971	6.81	47.971	4.797		
Lack-of-fit	5	45.163	6.41	45.163	9.033	16.08	0.004
Pure error	5	2.809	0.40	2.809	0.562		
Total	19	704.871	100.00				

Table 5: Analysis of Variance for tangential CF (Fz).

Source	DF	Seq SS	Contribution (%)	Adj SS	Adj MS	F value	P value
Model	9	140.666	94.35	140.666	15.6296	18.54	<0.0001
Linear	3	71.465	47.93	71.465	23.8216	28.26	<0.0001
κ_r	1	24.990	16.76	24.990	24.9902	29.64	<0.0001
γ_o	1	19.429	13.03	19.429	19.4289	23.05	0.001
λ_s	1	27.046	18.14	27.046	27.0458	32.08	<0.0001
Square	3	57.996	38.90	57.996	19.3319	22.93	<0.0001
κ_r * κ_r	1	26.842	18.00	25.541	25.5407	30.29	<0.0001
γ_o*γ_o	1	13.023	8.73	10.282	10.2818	12.20	0.006
λ_s*λ_s	1	18.131	12.16	18.131	18.1306	21.51	0.001
2-way interaction	3	11.205	7.52	11.205	3.7352	4.43	0.032
κ_r *γ_o	1	3.838	2.57	3.838	3.8378	4.55	0.059
κ_r *λ_s	1	5.420	3.64	5.420	5.4203	6.43	0.030
γ_o*λ_s	1	1.947	1.31	1.947	1.9474	2.31	0.160
Error	10	8.431	5.65	8.431	0.8431		
Lack-of-fit	5	4.289	2.88	4.289	0.8577	1.04	0.485
Pure error	5	4.142	2.78	4.142	0.8284		
Total	19	149.097	100.00				

Table 6: Analysis of variance for feed CF (Fx).

Source	DF	Seq SS	Contribution (%)	Adj SS	Adj MS	*F*-value	*P*-value
Model	9	297.886	95.43	297.886	33.098	23.21	<0.0001
Linear	3	38.470	12.32	38.470	12.823	8.99	0.003
κ_r	1	15.327	4.91	15.327	15.327	10.75	0.008
γ_o	1	2.412	0.77	2.412	2.412	1.69	0.223
λ_s	1	20.732	6.64	20.732	20.732	14.54	0.003
Square	3	256.976	82.32	256.976	85.659	60.06	<0.0001
κ_r * κ_r	1	74.165	23.76	97.153	97.153	68.12	<0.0001
γ_o*γ_o	1	177.831	56.97	181.792	181.792	127.46	<0.0001
λ_s*λ_s	1	4.980	1.60	4.980	4.980	3.49	0.091
2-way interaction	3	2.440	0.78	2.440	0.813	0.57	0.647
κ_r *γ_o	1	1.800	0.58	1.800	1.800	1.26	0.287
κ_r *λ_s	1	0.326	0.10	0.326	0.326	0.23	0.643
γ_o*λ_s	1	0.313	0.10	0.313	0.313	0.22	0.649
Error	10	14.262	4.57	14.262	1.426		
Lack-of-fit	5	10.144	3.25	10.144	2.029	2.46	0.172
Pure error	5	4.118	1.32	4.118	0.824		
Total	19	312.148	100.00				

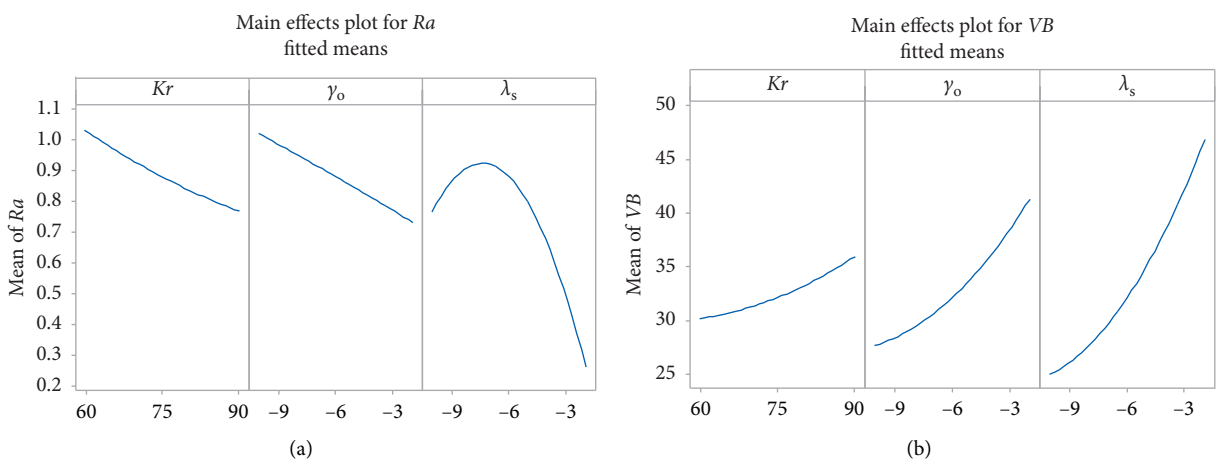

Figure 10: Main effect plots for (a) SR and (b) TW.

Table 7: Optimization results for desired SR, TW, and CF.

Response	Goal	Lower		Target	Upper	Weight	Importance
Ra	Target	0.252		0.734	1.020	1	1
VB	Target	22.200		25.000	50.260	1	1
F	Target	148.562		159.000	174.375	1	1
				Ra	*VB*	*F*	Composite
Solution	K_r	γ_o	λ_s	Fit	Fit	Fit	Desirability
1	75	−6	−10	0.734000	25.0000	159.000	1.00000

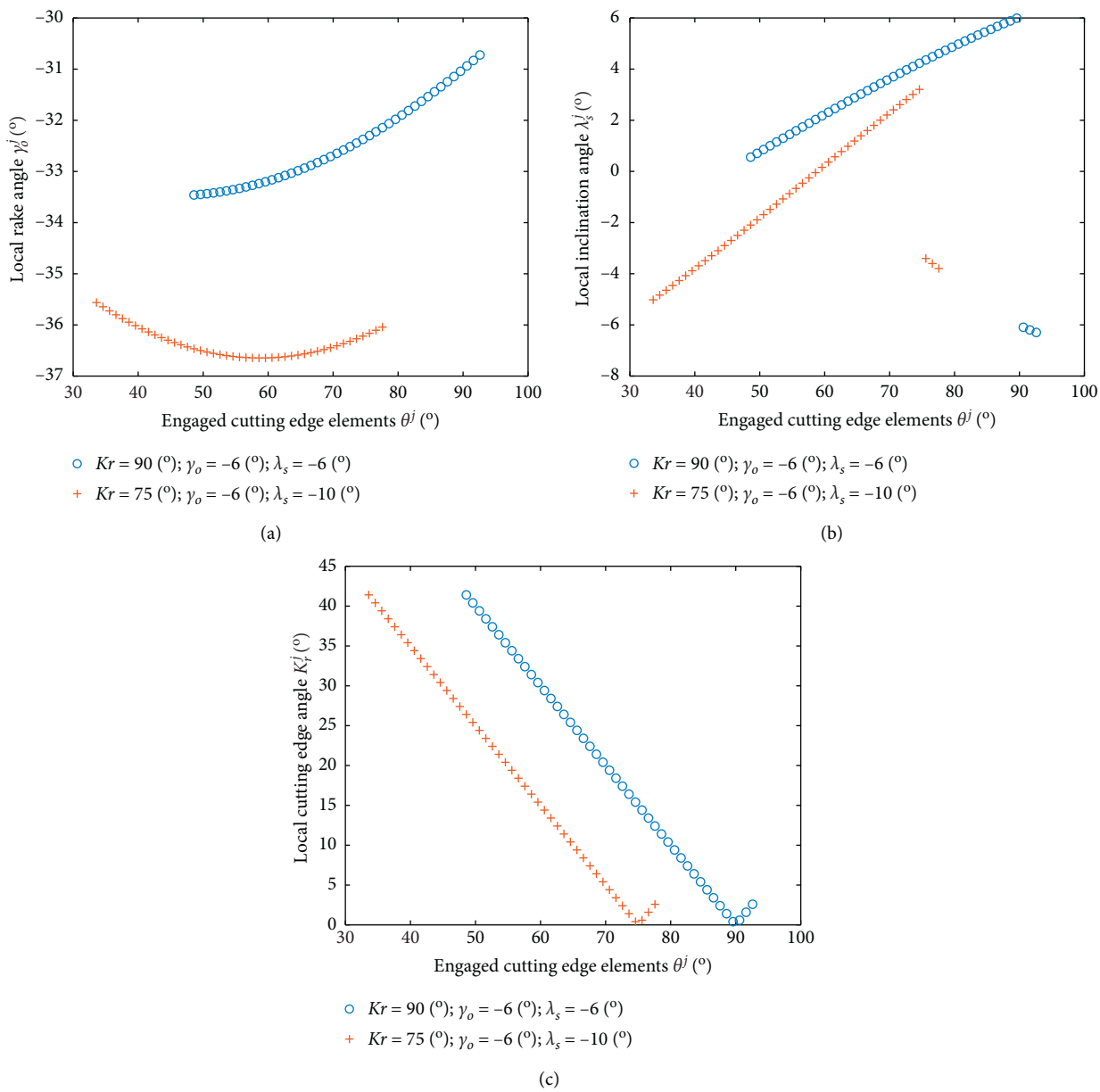

Figure 11: Comparison between standard and optimized local tool geometric parameters: (a) local RA, (b) local IA, and (c) local CEA.

Table 8: Optimization results for minimum SR, TW and CF.

Response	Goal	Lower		Target	Upper	Weight	Importance
Ra	Minimum			0.252	1.020	1	1
VB	Minimum			22.200	50.260	1	1
F	Minimum			148.56	174.38	1	1
				Ra	*VB*	*F*	Composite
Solution	K_r	γ_o	λ_s	Fit	Fit	Fit	Desirability
1	60	−10	−10	0.581563	17.4606	156.44	0.734796

Compared to using standard cutting tool angles, the optimal tool angles in Table 8 decreased SR and TW by 30.4% and 53.8%, respectively, while insignificantly increased CF by 1.7%.

5. Conclusion

Based on the proposed mathematical model and experimental results about the influences of tool geometry (CEA, RA, and IA) on performance characteristics (SR, TW, and CF) of hard turning, the main conclusions are drawn as follows.

The thrust force was the largest component of CF, followed by tangential force and feed force; and CF was too small to have meaningful effects on SR.IA was the most influential on CF (25.02%), followed by RA (14.26%) and CEA (10.04%). There were interaction effects between CEA, RA, and IA on CF. CF decreased with the increase in negative RA and IA. If IA increases higher than a certain value ($\lambda_s = -7.2^\circ$, with a minimum CF), CF increases after.

Increasing CEA resulted in changes in the cutting position on the tool-nose radius and hence decreased local negative RA (and correspondingly local CA). Increasing RA and IA also increased local negative RA. And, the changes of RA and IA mainly caused the changes of local IA and local RA, respectively.

Local RA and CA were the main factors that directly influenced performance characteristics (SR, TW, and CF) of hard turning. Increasing local negative RA resulted in higher SR and CF. Meanwhile, increasing local CA resulted in lower SR, TW, and CF. Under certain conditions, the positive influences of local CA outplayed the negative influences of local negative RA, thus decreasing SR and TW.

Local RA (and correspondingly local CA) was affected the most by IA, followed by RA and CEA. Therefore, IA is the most crucial tool angle for hard turning, followed by RA and CEA. At the same time, it is known that RA is the most influential factor in conventional turning. Compared to standard cutting tool angles, the optimal tool angles in our work significantly reduced SR and TW.

The proposed new mathematical model can be combined with formulas and other mathematical models to calculate local CF, cutting temperature, and TW for each cutting-edge element and the overall hard turning process. The analytical results of the mathematical model were in accordance with the experimental results.

Data Availability

The data used to support the findings of this study are included within the article.

Conflicts of Interest

The authors declare that they have no conflicts of interest.

References

[1] J. P. Davim, *Machining of Hard Materials*, Verlag London Limited: Springer, London, UK, 2011.

[2] M. D. Pham, H. G. Le, and D. D. Mai, "An experimental study on the effect of tool geometry on tool wear and surface roughness in hard turning," *Advances in Mechanical Engineering*, vol. 12, no. 9, pp. 1–11, 2020.

[3] H. Gökkaya and M. Nalbant, "The effects of cutting tool geometry and processing parameters on the surface roughness of AISI 1030 steel," *Materials & Design*, vol. 28, no. 2, pp. 717–721, 2007.

[4] M. Günay, İ. Korkut, E. Aslan, and U. Şeker, "Experimental investigation of the effect of cutting tool rake angle on main cutting force," *Journal of Materials Processing Technology*, vol. 166, no. 1, pp. 44–49, 2005.

[5] P. Cao, Z. Zhu, D. Buck, X. Guo, M. Ekevad, and X. A. Wang, "Effect of rake angle on cutting performance during machining of stone-plastic composite material with polycrystalline diamond cutters," *Journal of Mechanical Science and Technology*, vol. 33, no. 1, pp. 351–356, 2019.

[6] O. Zerti, M. A. Yallese, R. Khettabi, K. Chaoui, and T. Mabrouki, "Design optimization for minimum technological parameters when dry turning of AISI D3 steel using Taguchi method," *International Journal of Advanced Manufacturing Technology*, vol. 89, no. 5–8, pp. 1915–1934, 2017.

[7] S. K. Harisha, G. R. Rajkumar, V. Pawar, and M. Keshav, "Statistical investigation of tool geometry for minimization of cutting force in turning of hardened steel," *Materials Today: Proceedings*, vol. 5, no. 5, pp. 11277–11282, 2018.

[8] H. Saglam, F. Unsacar, and S. Yaldiz, "Investigation of the effect of rake angle and approaching angle on main cutting force and tool tip temperature," *International Journal of Machine Tools and Manufacture*, vol. 46, no. 2, pp. 132–141, 2006.

[9] D. Singh and P. V. Rao, "Optimization of tool geometry and cutting parameters for hard turning," *Materials and Manufacturing Processes*, vol. 22, no. 1, pp. 15–21, 2007.

[10] S. Neseli, S. Yaldız, and E. Türkes, "Optimization of tool geometry parameters for turning operations based on the response surface methodology," *Measurement*, vol. 44, pp. 580–587, 2011.

[11] V. S. Sharma, S. Dhiman, R. Sehgal, and S. K. Sharma, "Estimation of cutting forces and surface roughness for hard turning using neural networks," *Journal of Intelligent Manufacturing*, vol. 19, no. 4, pp. 473–483, 2008.

[12] A. K. Sahoo and B. Sahoo, "Experimental investigations on machinability aspects in finish hard turning of AISI 4340 steel using uncoated and multilayer coated carbide inserts," *Measurement*, vol. 45, no. 8, pp. 2153–2165, 2012.

[13] J. M. Zhou, H. Walter, M. Andersson, and J. E. Stahl, "Effect of chamfer angle on wear of PCBN cutting tool," *International Journal of Machine Tools and Manufacture*, vol. 43, no. 3, pp. 301–305, 2003.

[14] T. Zhao, J. M. Zhou, V. Bushlya, and J. E. Ståhl, "Effect of cutting edge radius on surface roughness and tool wear in hard turning of AISI 52100 steel," *The International Journal of Advanced Manufacturing Technology*, vol. 91, no. 9-12, pp. 3611–3618, 2017.

[15] H. Xu, H. Zhou, Z. Ma et al., "The influence of tool rake surface geometry on the hard turning process of AISI52100 hardened steel," *Materials*, vol. 12, no. 19, p. 3096, 2019.

[16] S. Wojciechowski, T. Chwalczuk, P. Twardowski et al., "Modeling of cutter displacements during ball end milling of inclined surfaces," *Archives of Civil and Mechanical Engineering*, vol. 5, no. 14, pp. 798–805, 2015.

[17] R. Suresh and S. Basavarajappa, "Effect of process parameters on tool wear and surface roughness during turning of

hardened steel with coated ceramic tool," *Procedia Materials Science*, vol. 5, pp. 1450–1459, 2014.

[18] W. B. Rashid, S. Goel, J. P. Davim, and S. N. Joshi, "Parametric design optimization of hard turning of AISI 4340 steel (69 HRC)," *The International Journal of Advanced Manufacturing Technology*, vol. 82, no. 1–4, pp. 451–462, 2016.

[19] A. Kumar, M. M. Mahapatra, and P. K. Jha, "Effect of machining parameters on cutting force and surface roughness of in situ Al–4.5%Cu/TiC metal matrix composites," *Measurement*, vol. 48, pp. 325–332, 2014.

[20] S. Khamel, N. Ouelaa, and K. Bouacha, "Analysis and prediction of tool wear, surface roughness and cutting forces in hard turning with CBN tool," *Journal of Mechanical Science and Technology*, vol. 26, no. 11, pp. 3605–3616, 2012.

[21] A. Zerti, M. A. Yallese, I. Meddour, S. Belhadi, A. Haddad, and T. Mabrouki, "Modeling and multi-objective optimization for minimizing surface roughness, cutting force, and power, and maximizing productivity for tempered stainless steel AISI 420 in turning operations," *The International Journal of Advanced Manufacturing Technology*, vol. 102, no. 1-4, pp. 135–157, 2019.

[22] A. Chabbi, M. A. Yallese, M. Nouioua, I. Meddour, T. Mabrouki, and F. Girardin, "Modeling and optimization of turning process parameters during the cutting of polymer (POM C) based on RSM, ANN, and DF methods," *The International Journal of Advanced Manufacturing Technology*, vol. 91, no. 5-8, pp. 2267–2290, 2017.

[23] A. Laouissi, M. A. Yallese, A. Belbah, S. Belhadi, and A. Haddad, "Investigation, modeling, and optimization of cutting parameters in turning of gray cast iron using coated and uncoated silicon nitride ceramic tools. Based on ANN, RSM, and GA optimization," *The International Journal of Advanced Manufacturing Technology*, vol. 101, no. 1-4, pp. 523–548, 2018.

[24] S. A. Bagaber and A. R. Yusoff, "Multi-objective optimization of cutting parameters to minimize power consumption in dry turning of stainless steel 316," *Journal of Cleaner Production*, vol. 157, pp. 30–46, 2019.

[25] X. Sun, Z. Shi, and J. Zhu, "Multi-objective design optimization of an ipmsm for evs based on fuzzy method and sequential taguchi method," *IEEE Transactions on Industrial Electronics*, p. 1, 2020.

[26] X. Sun, Z. Shi, G. Lei, Y. Guo, and J. Zhu, "Multi-objective design optimization of an ipmsm based on multilevel strategy," *IEEE Transactions on Industrial Electronics*, vol. 68, no. 1, pp. 139–148, 2021.

[27] V. Bushlya, F. Schultheiss, O. Zhou, and J.-E. Ståhl, "On the analytical representation of chip area and tool geometry when oblique turning with round tools. Part 2: variation of tool geometry along the edge line," *Procedia CIRP*, vol. 31, pp. 423–428, 2015.

[28] H. Khlifi, L. Abdellaoui, and W. Bouzid Sai, "An equivalent geometry model for turning tool with nose and edge radii," *The International Journal of Advanced Manufacturing Technology*, vol. 103, no. 9-12, pp. 4233–4251, 2019.

[29] K. Orra and S. K. Choudhury, "Mechanistic modelling for predicting cutting forces in machining considering effect of tool nose radius on chip formation and tool wear land," *International Journal of Mechanical Sciences*, vol. 142-143, pp. 255–268, 2018.

[30] L. Abdellaoui and W. Bouzid, "Thermomechanical modeling of oblique turning in relation to tool-nose radius," *Machining Science And Technology*, vol. 20, no. 4, pp. 586–614, 2016.

[31] A. Molinari and A. Moufki, "A new thermomechanical model of cutting applied to turning operations. part I. theory," *International Journal of Machine Tools and Manufacture*, vol. 45, no. 2, pp. 166–180, 2005.

[32] Z. Fu, X. Chen, J. Mao, and T. Xiong, "An analytical force mode applied to three-dimensional turning based on a predictive machining theory," *International Journal of Mechanical Sciences*, vol. 136, pp. 94–105, 2018.

[33] A. Anand, A. K. Behera, and S. R. Das, "An overview on economic machining of hardened steels by hard turning and its process variables," *Manufacturing Rev*, vol. 6, no. 4, 2019.

[34] J. P. Davim, *Computational Methods and Production Engineering*, Elsevier, Amsterdam, Netherlands, 2017.

[35] M. W. Azizi, S. Belhadi, M. A. Yallese, T. Mabrouki, and J.-F. Rigal, "Surface roughness and cutting forces modeling for optimization of machining condition in finish hard turning of AISI 52100 steel," *Journal of Mechanical Science and Technology*, vol. 26, no. 12, pp. 4105–4114, 2012.

[36] K. Bouacha, M. A. Yallese, S. Khamel, and S. Belhadi, "Analysis and optimization of hard turning operation using cubic boron nitride tool," *International Journal of Refractory Metals and Hard Materials*, vol. 45, pp. 160–178, 2014.

[37] V. P. Astakhov, *Geometry of Single-Point Turning Tools and Drills*, Springer, Berlin, Germany, 2010.